



PCCP

**Redox-Mediated Transformation of a $Tb_2O_3(111)$ Thin Film
from the Cubic Fluorite to Bixbyite Structure**

Journal:	<i>Physical Chemistry Chemical Physics</i>
Manuscript ID	CP-ART-09-2019-005083.R1
Article Type:	Paper
Date Submitted by the Author:	11-Nov-2019
Complete List of Authors:	Lee, Christopher; University of Florida, Department of Chemical Engineering Sayal, Ameen; University of Florida, Department of Chemical Engineering Vashishta, Saumye; University of Florida, Department of Chemical Engineering Weaver, Jason; University of Florida, Department of Chemical Engineering

SCHOLARONE™
Manuscripts

Redox-Mediated Transformation of a $\text{Tb}_2\text{O}_3(111)$ Thin Film from the Cubic Fluorite to Bixbyite Structure

Christopher J. Lee¹, Ameen Sayal¹, Saumye Vashishtha¹, Jason F. Weaver^{1*}

¹Department of Chemical Engineering, University of Florida, Gainesville, FL 32611, USA

*To whom correspondence should be addressed, weaver@che.ufl.edu

Tel. 352-392-0869, Fax. 352-392-9513

Abstract

We used temperature programmed desorption (TPD) and low energy electron diffraction (LEED) to investigate the isomeric structural transformation of a Tb_2O_3 thin film grown on Pt(111). We find that repeated oxidation and thermal reduction to 1000 K transforms an oxygen-deficient, cubic fluorite (CF) $\text{Tb}_2\text{O}_3(111)$ thin film to the well-defined bixbyite, or c- $\text{Tb}_2\text{O}_3(111)$ structure, whereas annealing the CF- $\text{Tb}_2\text{O}_3(111)$ film in UHV is ineffective in causing this structural transformation. We estimate that the final stabilized film consists of about ten layers of c- $\text{Tb}_2\text{O}_3(111)$ in the surface region plus about eight layers of CF- $\text{Tb}_2\text{O}_3(111)$ located between the c- $\text{Tb}_2\text{O}_3(111)$ and the Pt(111) substrate. Our measurements reveal the development of two distinct O_2 TPD peaks during the CF to bixbyite transformation that arise from oxidation of c- Tb_2O_3 domains to the stoichiometrically-invariant $\gamma\text{-Tb}_7\text{O}_{12}$ and $\delta\text{-Tb}_{11}\text{O}_{20}$ phases and demonstrate that the c- Tb_2O_3 phase oxidizes more readily than CF- Tb_2O_3 . We present evidence that nucleation and growth of c- Tb_2O_3 domains occurs at the buried $\text{TbO}_x/\text{CF-Tb}_2\text{O}_3$ interface, and that conversion of the interfacial CF- Tb_2O_3 to bixbyite takes place mainly during thermal reduction of TbO_x above ~ 900 K and causes newly-formed c- Tb_2O_3 to advance deeper into the film. The avoidance of low Tb oxidation states may facilitate the CF to bixbyite transformation via this redox mechanism.

Introduction

The rare earth oxides (REOs) exhibit favorable properties for various applications of oxidative catalysis including complete and partial oxidation,^{1,2} hydrogenation and dehydrogenation,³⁻⁵ coupling reactions,⁶⁻¹⁰ and the selective reduction of NO¹¹⁻¹³ to name a few.¹⁴⁻¹⁷ Though rare earth oxide surfaces can be effective in promoting various oxidation reactions, developing an understanding of the reaction mechanisms at the atomic level is challenging due to the highly dynamic nature of the REO structures and sensitivity to changes in oxidative environment.¹⁸⁻²⁰

Within the family of rare earth metals, only Ce, Pr, and Tb are known to form stable oxide phases beyond the sesquioxide (Ln_2O_3) and up to the dioxide (LnO_2) stoichiometry, allowing for the flexible storage and release of lattice oxygen necessary to facilitate redox chemistry. As lattice oxygen can participate directly in surface interactions through the Mars-van-Krevelen mechanism, sustained oxidative activity of these structures is largely dependent on their characteristic lattice oxygen mobility and ability to transform between reduced and oxidized phases.²¹⁻²³ This last note is especially promising for applications involving terbium oxide and praseodymium oxide since these oxides have the highest oxygen mobilities documented for REOs.²⁴ Bulk oxides of Tb, Pr and Ce can also form in stoichiometries that are intermediate to Ln_2O_3 and LnO_2 , with structures that feature either randomly-distributed oxygen vacancies or long-range ordered vacancies, depending upon conditions. These structures include a homologous series of well-defined intermediate phases in the form of $\text{Ln}_n\text{O}_{2n-2}$ ($n = 4, 6, 7, 9, 11, 12$, and ∞) in addition to a continuum of seemingly nonstoichiometric states adopting an oxygen-deficient fluorite structure.^{18,25}

Thin films of REOs grown on metal substrates have served as model systems for characterizing the surface structural and chemical properties of REOs, with ceria being the most widely studied REO thin film. These prior studies demonstrate that ceria oxidizes readily and forms the cubic

fluorite (CF) $\text{CeO}_2(111)$ structure on hexagonally close-packed metal surfaces during film growth in an O_2 background in UHV.²⁶⁻³² Thermal reduction of these $\text{CeO}_2(111)$ films as well as reduction by adsorbed reactants (e.g., CH_3OH) typically produces oxygen-deficient CF- $\text{CeO}_x(111)$ in which the oxygen vacancies are randomly distributed.^{23,33,34} Several reports show that solid-state reactions between layers of Ce metal and CeO_2 and also slow $\text{CeO}_x(111)$ reduction by H_2 can produce intermediate, stoichiometric CeO_x phases, including ordered structures of c- Ce_2O_3 , Ce_3O_5 and $\iota\text{-Ce}_7\text{O}_{12}$.³⁵⁻³⁸ Recent work also demonstrates that complete oxidation of an c- $\text{Pr}_2\text{O}_3(111)$ film followed by thermal reduction in UHV produces the h- $\text{Pr}_2\text{O}_3(0001)$ structure, thus enabling surface science investigations of distinct Pr_2O_3 surface structures.³⁹⁻⁴¹ These prior studies reveal that the development of intermediate, ordered phases of REO films can be quite sensitive to the film growth and redox conditions.

We have previously shown that terbia thin films grown on Pt(111) in an O_2 background form in the Tb_2O_3 stoichiometry and adopt a cubic fluorite (3×3) structure,¹⁶ in contrast to h- $\text{Pr}_2\text{O}_3(0001)$ ^{39,41-43} and $\text{CeO}_2(111)$ films prepared under similar conditions.^{20,35} Excellent lattice matching with the Pt(111) substrate likely stabilizes the CF-(3×3) structure of the CF- $\text{Tb}_2\text{O}_3(111)$ films and distinguishes the $\text{TbO}_x/\text{Pt}(111)$ thin film system from other reduced REO thin film systems. These Tb_2O_3 films can be oxidized extensively by O-atoms at 300 K, allowing for variation in oxidation state of the system.¹⁵ However, this prior work shows that oxidation of CF- Tb_2O_3 leads directly to CF- TbO_x without the formation of well-defined intermediate phases such as the iota and delta phases, and that thermal reduction at ~ 900 K restores the oxygen-deficient CF- Tb_2O_3 structure rather than generating the c- Tb_2O_3 phase that is preferred in bulk Tb_2O_3 .

In the present study, we report that a CF- $\text{Tb}_2\text{O}_3(111)$ film on Pt(111) transforms to a well-ordered bixbyite c- $\text{Tb}_2\text{O}_3(111)$ structure after repeated oxidation and thermal reduction to 1000 K,

whereas the CF-Tb₂O₃(111) structure remains unchanged during prolonged annealing in UHV. We further present evidence that oxidation of the c-Tb₂O₃(111) film occurs more readily than CF-Tb₂O₃(111) and occurs through the sequential formation of the stoichiometric iota (ι-Tb₇O₁₂) and delta (δ-Tb₁₁O₂₀) phases. Our results reveal that additional lattice oxygen accommodated within the film facilitates the transition between the isomeric CF and bixbyite Tb₂O₃(111) structures, and may shed light into the nature of lattice oxygen exchange in other sesquioxides within the family of REOs.

Experimental Details

Experiments for this study were carried out in a three-level ultrahigh vacuum (UHV) chamber with a typical base pressure of 2×10^{-10} Torr. The details for this system are documented in prior studies.⁴⁴⁻⁴⁶ Briefly, the chamber is equipped with a RF plasma source (Oxford Scientific Instruments) for generating atomic oxygen beams, a low energy electron diffraction (LEED) optics (SPECS) for characterization of surface structure, a quadrupole mass spectrometer (QMS) (Hiden) for temperature-programmed desorption (TPD) measurements, and a dual Mg/Al anode X-ray source and hemispherical analyzer (SPECS) for X-ray photoelectron spectroscopy (XPS) measurements. The plasma source is housed in a two-stage differentially-pumped beam chamber that connects to the UHV analysis chamber.

The Pt(111) crystal utilized in this study is a circular disk (10 mm x 1 mm) that was supported by tungsten wires fed through grooves located at the top and bottom edges of the crystal. The wires are held in thermal contact with a liquid nitrogen cooled copper reservoir and can be resistively heated. A type K thermocouple is spot welded to the back of the sample, and DC current supplied to the tungsten wires, regulated by a PID controller, allows for sample temperature control between

the range of ~89 K to 1100 K. We cleaned the sample by sputtering the surface with 600 eV Ar⁺ ions at an elevated temperature of 600 K and post annealing the sample to 1000 K. We also find that cycling the sample between 300 K and 1000 K in 5×10^{-7} Torr of O₂ is particularly effective at removing surface carbon and other adsorbed species. We considered the sample to be clean when we observed negligible levels of carbon and oxygen in XPS (C 1s and O 1s peaks) as well as negligible amounts of CO and CO₂ evolution during TPD.

We grew terbium oxide films by the reactive physical vapor deposition (RPVD) of terbium metal (Alfa Aesar, 99.9%) onto the clean Pt(111) substrate. We vaporized Tb metal from a Ta crucible using an e-beam evaporator (McAllister Technical services) and deposited in an O₂ background of 5×10^{-7} Torr. We held the sample at 600 K during deposition followed by post annealing of the film at 1000 K in the same oxygen background. This approach has proven to be effective for improving the overall crystallinity of the initial Tb₂O₃ film^{2,16,47} as well as preparing high-quality thin films of other rare earth oxides including Sm₂O₃(111)¹⁴ and CeO₂(111).⁴⁸ We estimate that the average deposition rate was 0.13 ± 0.02 layer/min of Tb₂O₃. In this study, one layer is defined in reference to bulk c-type Tb₂O₃ as the O-Tb-O trilayer separation in the [111] direction. This corresponds to a height of 3.01 Å and a Tb density of 8.57×10^{14} cm⁻² per layer. We estimated film thicknesses from measurements of the attenuation of the Pt 4f XPS peak intensity. We estimate an inelastic mean free path (IMFP) of 26.9 Å for the Pt 4f photoelectrons through TbO_x using an average of the IMFP values determined from the TPP-2M and Gries equations for an electron kinetic energy of 1415 eV.⁴⁹

We oxidized the Tb₂O₃ films using plasma-generated O-atom beams and investigated the oxidized films using LEED, XPS and TPD. We estimate an O-atom flux of 0.018 ML s⁻¹ for these experiments based on TPD measurements of oxygen uptake by Pt(111). We found that flashing

the TbO_x films to 900 K and 1000 K prior to any O atom exposures was sufficient to remove surface contamination and reduce the film to a reproducible level, consistent with the Tb_2O_3 stoichiometry (see below). After an O-atom exposure, we positioned the sample in front of a shielded mass spectrometer at a distance of ~ 5 mm and heated at a constant rate of 1 K/s until reaching a sample temperature of 900 or 1000 K. We estimate the absolute desorption yields of O_2 on the basis of O_2 TPD spectra taken after oxygen adsorption onto Pt(111). A saturation exposure to background O_2 at 300 K generates a (2×2) -O layer on Pt(111) with a coverage of 0.25 O-atoms per surface Pt atom. We estimate an uncertainty of about 5% in the absolute O_2 coverages based on this approach. We define 1 ML (monolayer) of O-atoms as equal to the density of Tb atoms in one O-Tb-O trilayer of $\text{TbO}_2(111)$, and report O_2 TPD yields in these units. This coverage scale provides a convenient metric for stoichiometric analysis as a single O-Tb-O trilayer of $\text{TbO}_2(111)$ contains 2 ML of O atoms and 1 ML of Tb atoms, and 0.5 ML of O-atoms are needed to completely oxidize a single trilayer of Tb_2O_3 to TbO_2 . We performed XPS experiments using Al $K\alpha$ X-rays and collected spectra using a hemispherical analyzer with a pass energy of 27 eV. The data here is presented after averaging 20 scans and applying a linear background subtraction over the range of collected spectra.

Results

Oxidation of CF- $\text{Tb}_2\text{O}_3(111)$

Figure 1a shows O_2 TPD traces obtained after oxidizing an ~ 18 -layer CF- $\text{Tb}_2\text{O}_3(111)$ film to varying extents at 300 K using an O-atom beam, and limiting the final temperature to 900 K during the measurements. Figure 1b shows the corresponding oxygen uptake by the CF film as a function of the exposure time. As mentioned in Experimental Details, we have previously shown that the

as-deposited Tb_2O_3 film forms in the oxygen-deficient CF structure, and that oxygen vacancies arrange into a (3×3) superstructure at the surface of films of thickness greater than ~ 5 layers (Figure 2a).¹⁶ We have also previously shown that CF- $\text{Tb}_2\text{O}_3(111)$ grows epitaxially on Pt(111) and adopts an $(3 \times 3)/(4 \times 4)$ coincident structure with minimal strain, and suggested that this favorable CF- $\text{Tb}_2\text{O}_3(111)/\text{Pt}(111)$ interface likely mediates formation of a (3×3) arrangement of surface vacancies in thick films.¹⁶ Similar to previous results,^{2,15} the O_2 TPD traces exhibit two broad features centered at 370 K and 670 K that have been attributed to oxygen evolving from the surface and bulk of the oxidized film, respectively. These features populate nearly simultaneously as a function of the total oxygen uptake. A small peak at 770 K also becomes evident as the oxygen uptake approaches saturation. We attribute this small peak to the decomposition of crystalline $\text{1-Tb}_7\text{O}_{12}$ domains in the bulk of the film (see below). We also note that the O_2 desorption rate remains appreciable at 900 K when the TPD experiment ends. This characteristic appears to play an important role in promoting restructuring as discussed below. Oxygen uptake by the CF film saturates at about 1.25 ML for oxidation at 300 K. This value is surprisingly low as it is equivalent to completely oxidizing only about 2.5 layers of Tb_2O_3 to TbO_2 , whereas we estimate that the film is about 18 layers thick. We thus conclude that only layers near the vacuum-oxide interface oxidize under the conditions studied.

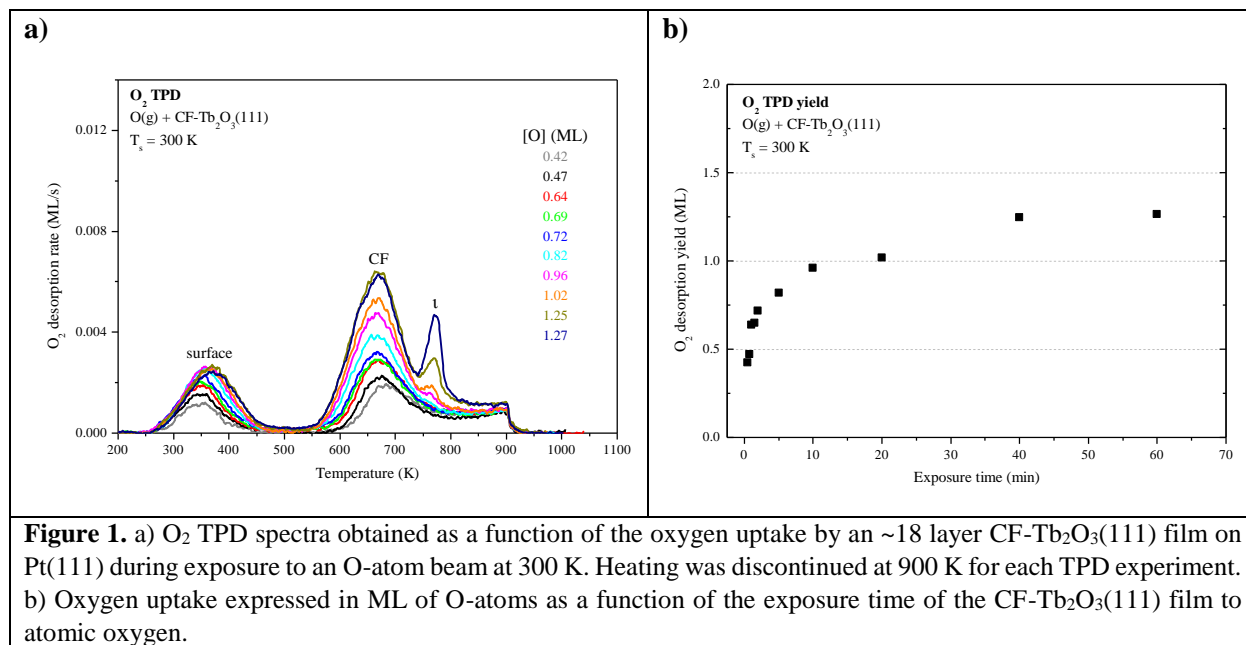


Figure 1. a) O_2 TPD spectra obtained as a function of the oxygen uptake by an ~ 18 layer $CF-Tb_2O_3(111)$ film on $Pt(111)$ during exposure to an O-atom beam at 300 K. Heating was discontinued at 900 K for each TPD experiment. b) Oxygen uptake expressed in ML of O-atoms as a function of the exposure time of the $CF-Tb_2O_3(111)$ film to atomic oxygen.

LEED from $TbO_x(111)$ structures

We find that repeated oxidation and reduction by heating to 1000 K during TPD induces a structural transformation of the $Tb_2O_3(111)$ film such that the cubic fluorite (CF) structure transforms into a well-ordered $c-Tb_2O_3(111)$ structure, i.e., bixbyite. We obtained the LEED patterns in Figures 2a,b from the initial $CF-Tb_2O_3(111)$ film and after oxidizing and reducing the film to 1000 K ten times, where each oxidation step was performed at 300 K and involved an O-atom exposure of ~ 60 ML. The initial $Tb_2O_3(111)$ surface exhibited a (3×3) pattern with broad spots (Figure 2a), consistent with our earlier findings.¹⁶ While the $CF-(3 \times 3)$ structure persists after annealing to 1000 K in UHV or low O_2 pressures, the $Tb_2O_3(111)$ surface obtained after the repeated oxidation/reduction steps (10x) exhibits a sharp (4×4) LEED pattern in the $CF-TbO_x(111)$ basis (Figure 2b) consistent with $c-Tb_2O_3(111)$. Prior studies report that the $c-Ce_2O_3(111)$ surface also generates a (4×4) LEED pattern.^{34,35,37} The $c-Tb_2O_3(111)$ unit cell exhibits three-fold symmetry, resembling a hexagonal lattice, with lattice constants that are four

times larger than the CF-TbO_x(111) unit cell,¹⁸ and thus gives a (4 × 4) LEED pattern in the TbO_x(111) basis. The much sharper spots in the (4 × 4) vs. (3 × 3) LEED pattern indicate that the oxidation/reduction steps improve the crystallinity of the Tb₂O₃ film such that the crystalline domains of the bixbyite structure are larger than those of the original cubic fluorite structure. Figures 2c,d show LEED patterns obtained after oxidizing the c-Tb₂O₃(111) film under different conditions, as discussed below.

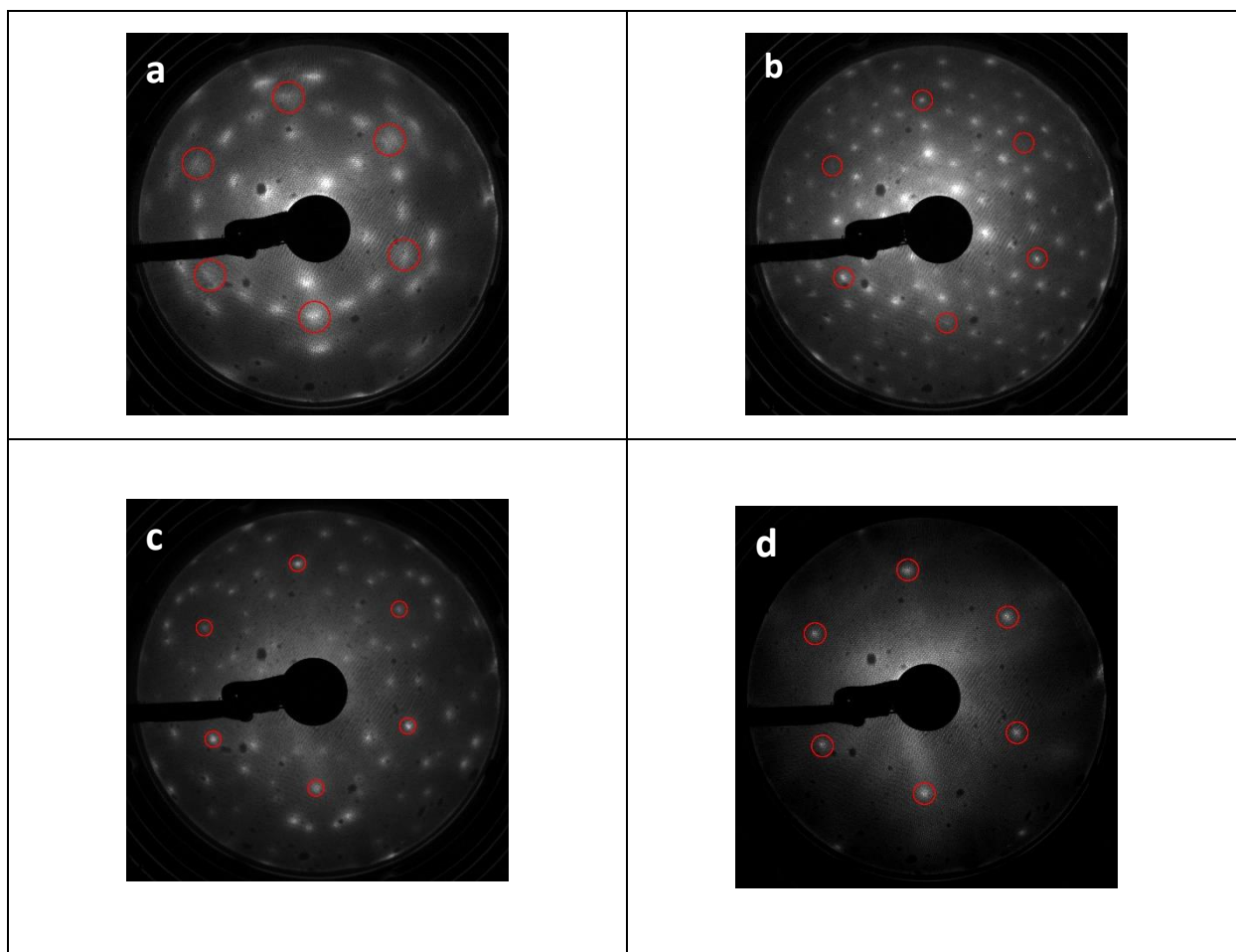


Figure 2. Development of stable bixbyite Tb₂O₃ film and higher ordered intermediate structures. Reference LEED images taken at 95 eV shown after (a) initial RPVD of 18 trilayer (3 × 3) CF-Tb₂O₃(111) film, (b) (4 × 4) c-Tb₂O₃(111) structure obtained after ten cycles of O-atom exposure followed by TPD from 300 to 1000 K, (c) ($\sqrt{7} \times \sqrt{7}$)R19.1° structure for t-Tb₇O₁₂(111) observed after 20 minute O-atom exposure at 300 K, and heating to 700 K, and (d) TbO₂(111) film stabilized by 20 minute O-atom exposure at 300 K. The circles mark the reciprocal space positions of the CF-TbO_x(111)-(1 × 1) unit cell.

O₂ TPD during the cubic fluorite to bixbyite Tb₂O₃(111) transformation

We collected an O₂ TPD spectrum after each oxidation treatment to monitor how the oxygen uptake and desorption behavior evolve as the film transforms from CF to bixbyite. Figure 3a shows O₂ TPD spectra obtained after successively oxidizing the Tb₂O₃(111) film by exposure to 60 ML O-atoms at 300 K, and allowing the final temperature to reach 1000 K during each TPD measurement while Figure 3b shows the corresponding oxygen uptake. The TPD features arising from bulk oxide decomposition change significantly with each oxidation step, until stabilizing after ten steps. After the first oxidation step, bulk oxide decomposition produces a broad feature centered at about 670 K and a small peak (ι -peak) at 770 K. Repeated oxidation and reduction causes the ι -peak and a second peak (δ -peak) initially at 634 K to intensify significantly, while the desorption rate between these peaks diminishes. The δ and ι peaks upshift slightly after successive oxidation/reduction treatments and appear at 643 K and 781 K after the ninth experiment when the O₂ TPD spectra appear to stabilize. A third feature (α -feature) at ~580 K also develops on the leading edge of the δ -peak that is less intense and broader than the δ and ι peaks. The O₂ TPD spectra change only slightly upon repeated exposure to ~60 ML of O-atoms and reduction after the 10th step, and we observe a small increase (< 0.1 ML) in the TPD yield in the α -feature after conducting an ~120 ML O-atom exposure once the c-Tb₂O₃ film stabilized (see SI). These observations demonstrate that the CF to c-Tb₂O₃ transformation effectively reaches completion after 10 redox steps, but that oxygen atoms can slowly populate the α -state at larger exposures.

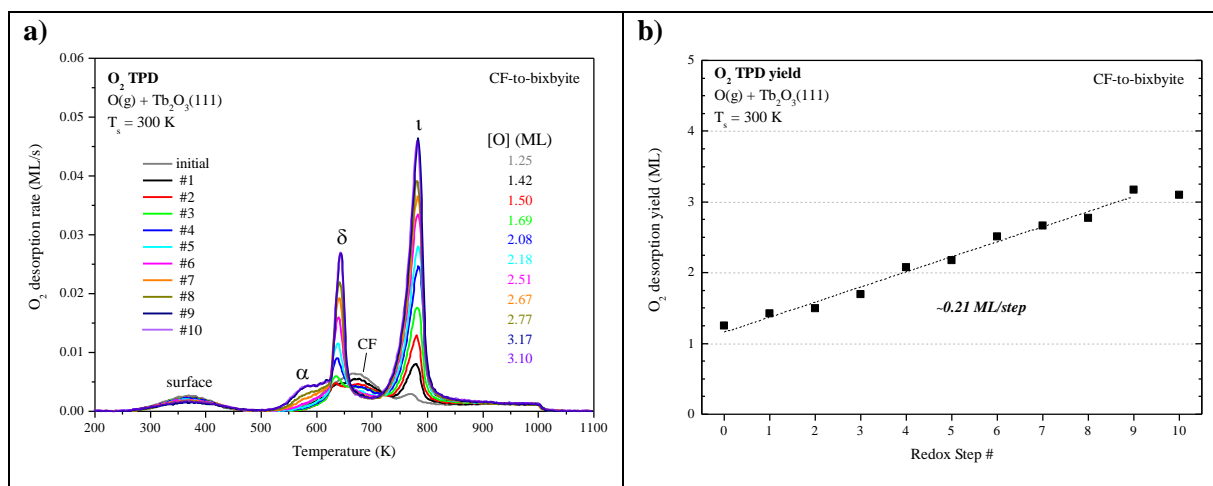


Figure 3. Transformation of an 18 ML CF-Tb₂O₃ (111) structure to c-Tb₂O₃(111) by repeated oxidation and reduction during TPD from 250-1000 K. (a) Progression of O₂ TPD spectra obtained after repeatedly exposing the Tb₂O₃(111) film to ~60 ML of O-atoms at 300 K, and reducing the film during TPD. (b) Oxygen uptake estimated from O₂ TPD yields as function of successive redox steps.

We attribute the δ and ι TPD peaks to phase transformations in the bulk wherein the stoichiometrically well-defined phases, δ -Tb₁₁O₂₀ and ι -Tb₇O₁₂, decompose via the general reactions, δ -Tb₁₁O₂₀ \rightarrow ι -Tb₇O₁₂ + O₂(g) and ι -Tb₇O₁₂ \rightarrow c-Tb₂O₃ + O₂(g), respectively. Support for this interpretation comes firstly from comparison with prior studies which report that the decomposition of TbO_x powders, oxidized at 973 K, yields two sharp O₂ TPD peaks near ~673 and 950 K arising from reduction of the δ and ι phases, respectively.^{21,50,51} The ι -phase decomposes at considerably higher temperature (950 vs. 780 K) in these prior studies compared with our results for the oxidized TbO_x film. A viable explanation is that the higher oxidation temperatures used in previous work allows the ι -phase to more fully equilibrate and become more stable compared with the ι -phase that forms in the present experiments. The narrowness of the δ and ι TPD peaks that we observe is indicative of phase change of compositionally-invariant compounds, and suggests that decomposition of the δ and ι phases rather than oxygen diffusion to the surface controls the rates of O₂ desorption under the conditions studied. LEED observations also support our assignment of the ι TPD peak. We obtained the LEED pattern shown in Figure 2c after extensively

oxidizing the TbO_x film, followed by heating to 700 K to isolate the state responsible for the ι TPD peak. This surface exhibits a sharp $(\sqrt{7} \times \sqrt{7})R19.1^\circ$ LEED pattern that is characteristic of the ι - $\text{Tb}_7\text{O}_{12}(111)$ structure, similar to prior results for ceria.^{36,52,53}

In contrast, however, we were unable to observe a distinct LEED pattern for δ - $\text{Tb}_{11}\text{O}_{20}$ after several attempts to isolate this phase and improve its crystallinity, including heating to 600 K as well as cycling the surface temperature between 600 and 630 K during oxidation. We speculate that either the crystalline domains of the δ - $\text{Tb}_{11}\text{O}_{20}$ phase remain too small after heating to ~ 600 K to yield an observable LEED pattern, or that the δ -phase was predominantly located in the subsurface. Finally, we observe a sharp (1×1) pattern superposed on a diffuse background after fully oxidizing the TbO_x film at 300 K (Figure 2d). The emergence of the (1×1) pattern suggests that the 60 ML O-atom exposures cause the surface to oxidize toward the TbO_2 stoichiometry, and generate a cubic fluorite (111) surface lattice. We attribute the small α TPD feature to the decomposition of domains of a disordered α - TbO_x phase with oxygen content close to or higher than the δ -phase, i.e., $x > \sim 1.8$. The analysis presented below clarifies how we estimate the overall stoichiometry of the film as given by the coefficient x . A key finding is that the development of the sharp δ and ι TPD peaks coincide with the transformation of CF- Tb_2O_3 to c- Tb_2O_3 . These changes demonstrate that oxidation of the c- Tb_2O_3 structure results in the formation of crystalline structures with specific stoichiometry (δ - $\text{Tb}_{11}\text{O}_{20}$ and ι - Tb_7O_{12}) and long-range ordering of oxygen vacancies, rather than a CF- TbO_x phase with variable O-density, at least up to a local oxygen concentration of $x = 1.818$. We emphasize that our TPD results demonstrate that the intermediate stoichiometric phases develop either at 300 K or as the sample is heated during TPD, at temperatures below that at which the phases decompose, because TPD provides information about

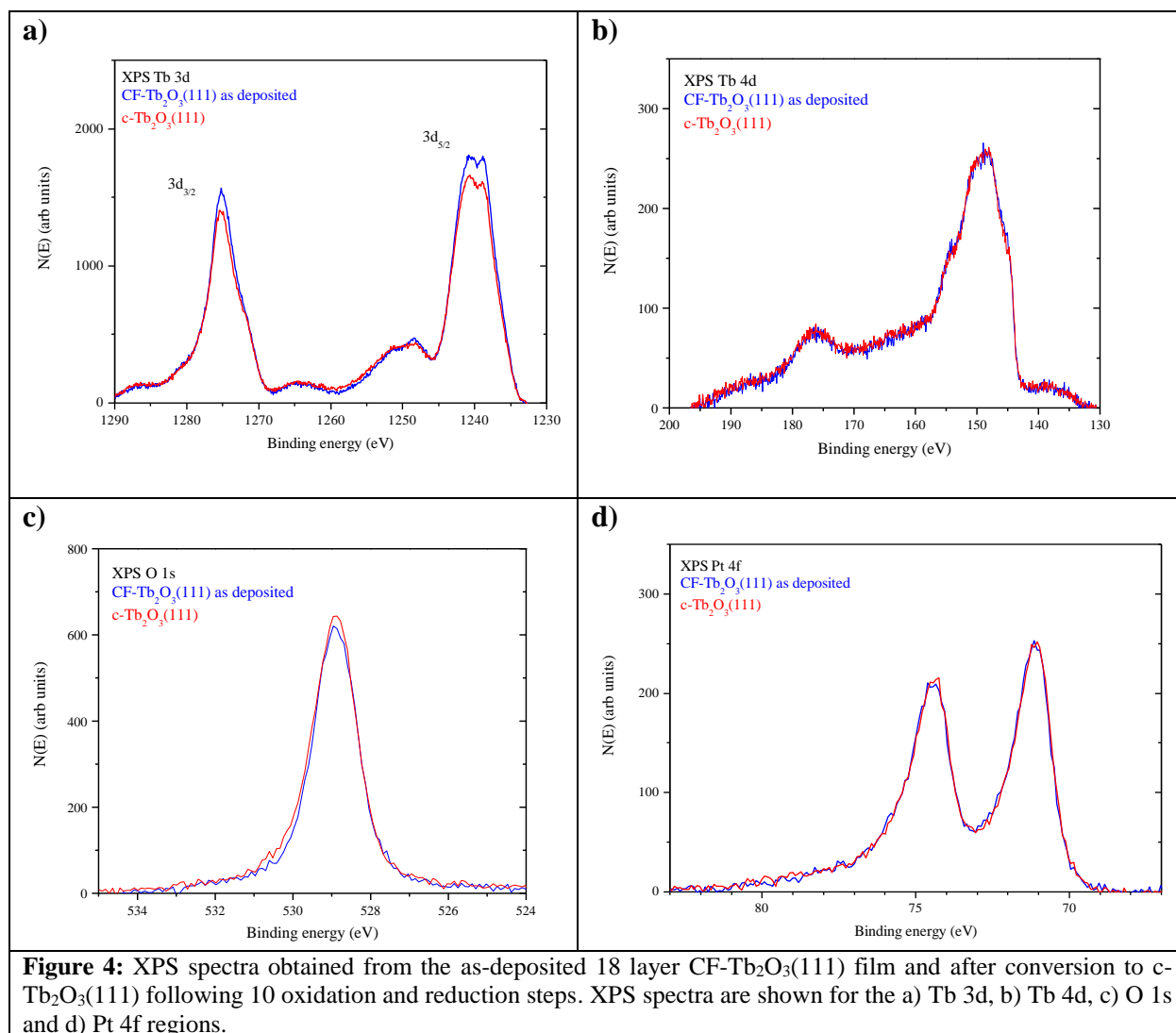
the decomposition rather than formation of the TbO_x phases. We speculate that the intermediate phases initially form during oxidation of $c-Tb_2O_3$ domains at 300 K but that these phases further develop with increasing temperature on the timescale ($\sim 300-400$ sec) of the TPD measurements.

Figure 3b shows that oxygen uptake by the film increases steadily after successive oxidation/reduction steps, until apparently stabilizing after the ninth step. The oxygen uptake is 1.25 ML for the initial CF- $Tb_2O_3(111)$ film and increases by ~ 0.1 to 0.3 ML in each successive step, reaching a value of 3.1 ML during the tenth O-atom exposure. These results demonstrate that conversion of oxygen-deficient, CF- Tb_2O_3 to the $c-Tb_2O_3$ structure enhances (by 250%) the oxygen uptake by the film in addition to generating the intermediate $\delta-Tb_{11}O_{20}$ and $t-Tb_7O_{12}$ phases. These observations lead to two key conclusions, namely, that oxidation of $c-Tb_2O_3$ is more facile than CF- Tb_2O_3 under the conditions studied and that the $c-Tb_2O_3$ structure advances into the film during reduction of oxidized TbO_x and enables additional oxygen uptake.

XPS characterization of cubic fluorite and $c-Tb_2O_3(111)$

Figures 4a-d show XPS Tb 3d, Tb 4d, O 1s and Pt 4f spectra obtained from the as-deposited CF- $Tb_2O_3(111)$ film and after completing 10 redox steps to transform the film to the $c-Tb_2O_3(111)$ structure, as described above. The Tb 3d and 4d spectra agree well with previously reported XPS data reported for a CF- $Tb_2O_3(111)$ film. The main peaks in the Tb 3d spectra are slightly less intense ($\sim 5\%$) for the $c-Tb_2O_3(111)$ vs. CF- $Tb_2O_3(111)$ films, whereas the Tb 4d spectra overlap closely. We have previously shown that the intensity of the main Tb $3d_{5/2}$ (and $Tb_{3/2}$) peak relative to the feature located at ~ 10 eV higher binding energy decreases as TbO_x films becomes increasingly oxidized.^{2,15} Since the Tb 3d spectra are significantly more surface sensitive than the

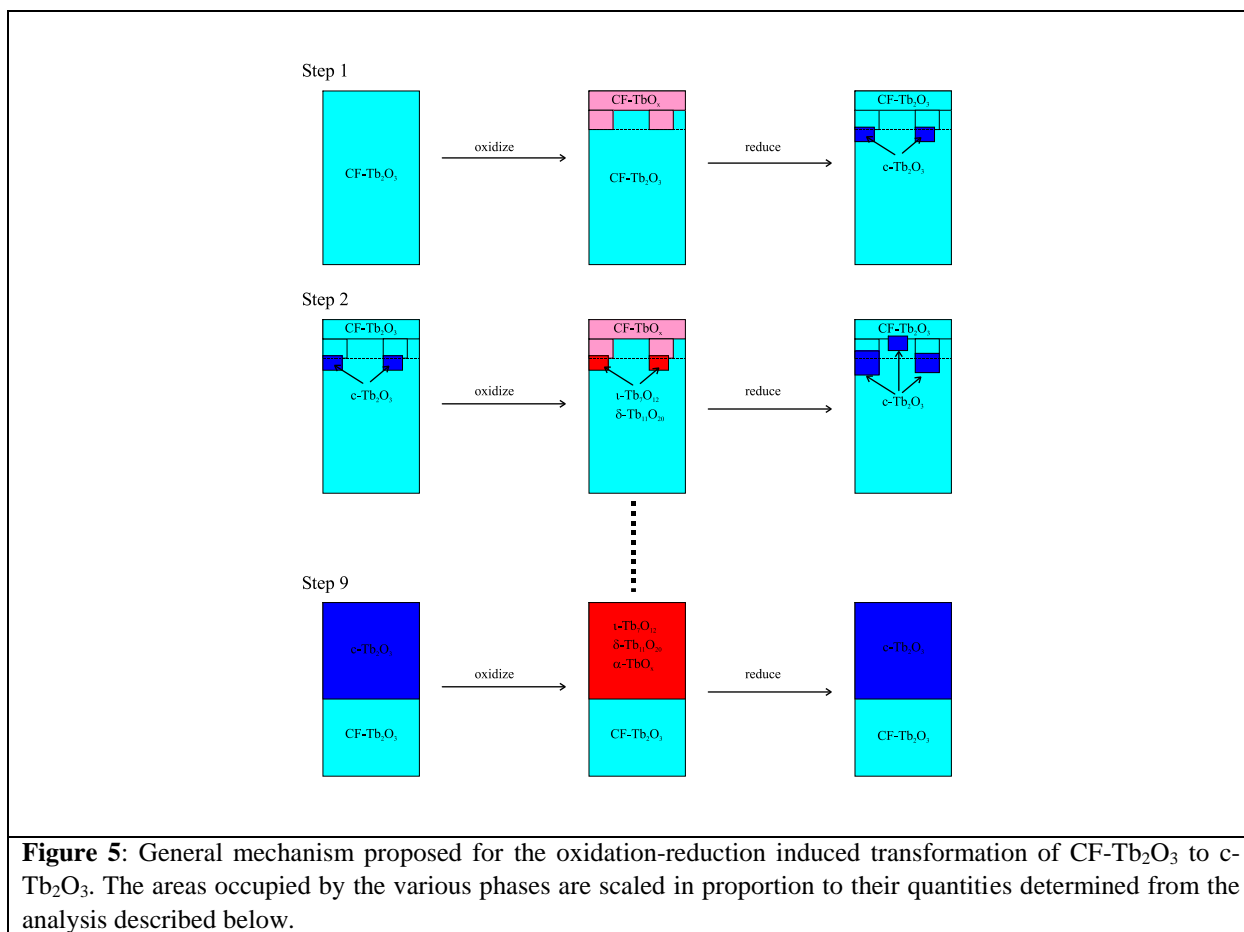
Tb 4d spectra at the photon energy used in our experiments, the lower intensity of the main Tb 3d peaks and the similarity in the Tb 4d spectra may indicate that the near surface region of the c-Tb₂O₃(111) film is slightly more oxidized than the CF-Tb₂O₃(111) film. Figure 4c shows that the O 1s peak is also slightly more intense (~7%) for the c-Tb₂O₃(111) vs. CF-Tb₂O₃(111) film. The differences in Tb 3d and O 1s spectra may indicate that the surface of the c-Tb₂O₃(111) film has a higher oxygen content than the CF-Tb₂O₃(111) film, but the differences are quite small and could arise from variations in background adsorption of H₂O during the measurements. Lastly, we find that the Pt 4f spectra are nearly identical for the CF-Tb₂O₃(111) and c-Tb₂O₃(111) films, demonstrating that film dewetting and Tb-Pt alloying occur negligibly during the TPD experiments. This finding is consistent with the higher thermal stability of Tb₂O₃ compared with Ce₂O₃¹⁸ as well as reports that thick CeO₂ films undergo negligible reduction upon heating to ~1000 K in UHV.^{17,54} Overall, our XPS results strongly support the conclusion that repeated oxidation and reduction transforms the CF-Tb₂O₃(111) to the bixbyite c-Tb₂O₃(111) structure while maintaining the sesquioxide stoichiometry.



Proposed general mechanism for c-Tb₂O₃ formation

Figure 5 illustrates the general mechanism that we propose to explain how CF-Tb₂O₃ transforms to c-Tb₂O₃ and increases the quantity of Tb₂O₃ which oxidizes. Consistent with observations, our model stipulates that oxidation of CF-Tb₂O₃ produces oxidized TbO_x only in the layers near the vacuum-oxide interface, leaving the underlying layers in reduced form (Figure 5). We propose that the bixbyite phase nucleates near the TbO_x-Tb₂O₃ interface during thermal reduction of the

oxidized region, and incorporates material from the underlying CF-Tb₂O₃ as well as the near-surface region that was originally oxidized (Step 1). As a result, the newly-formed bixbyite seeds penetrate into layers both above and below the TbO_x-Tb₂O₃ interface that forms during the first oxidation step. We emphasize that the large increase in total oxygen uptake observed during the CF to c-Tb₂O₃ transformation (Figure 3b) provides clear evidence that CF-Tb₂O₃ regions that remain unoxidized, after the O-atom exposures, transform to the c-Tb₂O₃ phase either before or, more likely, during subsequent thermal reduction.



According to the proposed mechanism, a subsequent oxygen exposure causes oxidation of both the near-surface CF-Tb₂O₃ layers and the c-Tb₂O₃ seeds, with more facile oxidation of c-Tb₂O₃

causing a net increase in the total oxygen uptake in Step 2 compared with Step 1 as well as subsequent steps. Our results suggest that oxidation of CF-Tb₂O₃ increases the oxygen content of this region while maintaining the CF structure, whereas oxidation sequentially transforms the bixbyite seeds into ι -Tb₇O₁₂ followed by δ -Tb₁₁O₂₀ and α -TbO_x. Below we present additional analysis showing that oxidation of c-Tb₂O₃ produces mixtures of these oxidized phases. Subsequent thermal reduction then causes the c-Tb₂O₃ grains to further increase in size and may also induce additional c-Tb₂O₃ nucleation. The appearance of a sharp (4 × 4) LEED pattern provides evidence that the c-Tb₂O₃ grains grow significantly and reach the surface after repeated redox steps (Figure 2b). Growth of the c-Tb₂O₃ domains by this mechanism would cause the c-Tb₂O₃/CF-Tb₂O₃ interface to advance deeper into the solid (Figure 5), and would steadily enhance the oxygen uptake given that c-Tb₂O₃ oxidizes more efficiently than CF-Tb₂O₃ according to our data. We note that Figure 5 shows formation of c-Tb₂O₃ only in the subsurface during the first two redox steps, but our results indicate that large c-Tb₂O₃(111) domains also form at the surface during the later stages of the transformation (e.g., Step 9, Figure 5). Again, we emphasize that the TPD results probe decomposition of the oxide phases rather than formation and thus only provide evidence that the intermediate ordered oxide phases form at temperatures below that at which they decompose during TPD. A possibility is that vacancy reordering is limited during oxidation of c-Tb₂O₃ domains at 300 K and that the ordered ι and δ phases develop more fully within these domains as the film temperature increases during the timescale of the TPD measurements.

We emphasize that reducing the oxidized TbO_x film to a final temperature of 1000 K rather than 900 K strongly promotes the CF to bixbyite transformation, whereas repeatedly annealing the reduced, CF-Tb₂O₃ films to 1000 K in UHV has been ineffective in promoting the transformation.¹⁶ This behavior suggests that c-Tb₂O₃ formation occurs primarily toward the end

of the thermal reduction experiment, when oxygen atoms are continuing to slowly vacate the film. In fact, we estimate that ~ 0.15 ML of oxygen desorbs between 900 K and 1000 K during each TPD experiment, where this oxygen yield agrees closely with the ~ 0.2 ML increase in oxygen uptake per oxidation/reduction step (Figure 3b). The agreement between these values further supports the idea that bixbyite formation occurs mainly above 900 K during reduction of a small fraction of remaining oxidized TbO_x . These findings suggest that oxygen removal above 900 K occurs by a mechanism that promotes vacancy ordering and the transformation of cubic fluorite to bixbyite Tb_2O_3 .

Quantification of the oxide phase distribution

We analyzed the O_2 TPD spectra to estimate how the oxygen desorption yields and oxide phase distribution evolve as a function of successive oxidation/reduction steps of the TbO_x film. In our analysis, we fit each O_2 TPD trace with three peaks representing desorption from the δ -phase, the ι -phase and the oxidized CF- TbO_x phase, respectively, and computed the desorption yield for each peak. We approximate the oxygen yield in the α TPD feature as the difference between the O_2 TPD yield measured above ~ 450 K and that determined from our fits of the remaining TPD features, i.e., $\iota + \delta + \text{CF}$. The SI provides details of our approximate deconvolution approach and shows representative fits of O_2 TPD spectra analyzed in the study.

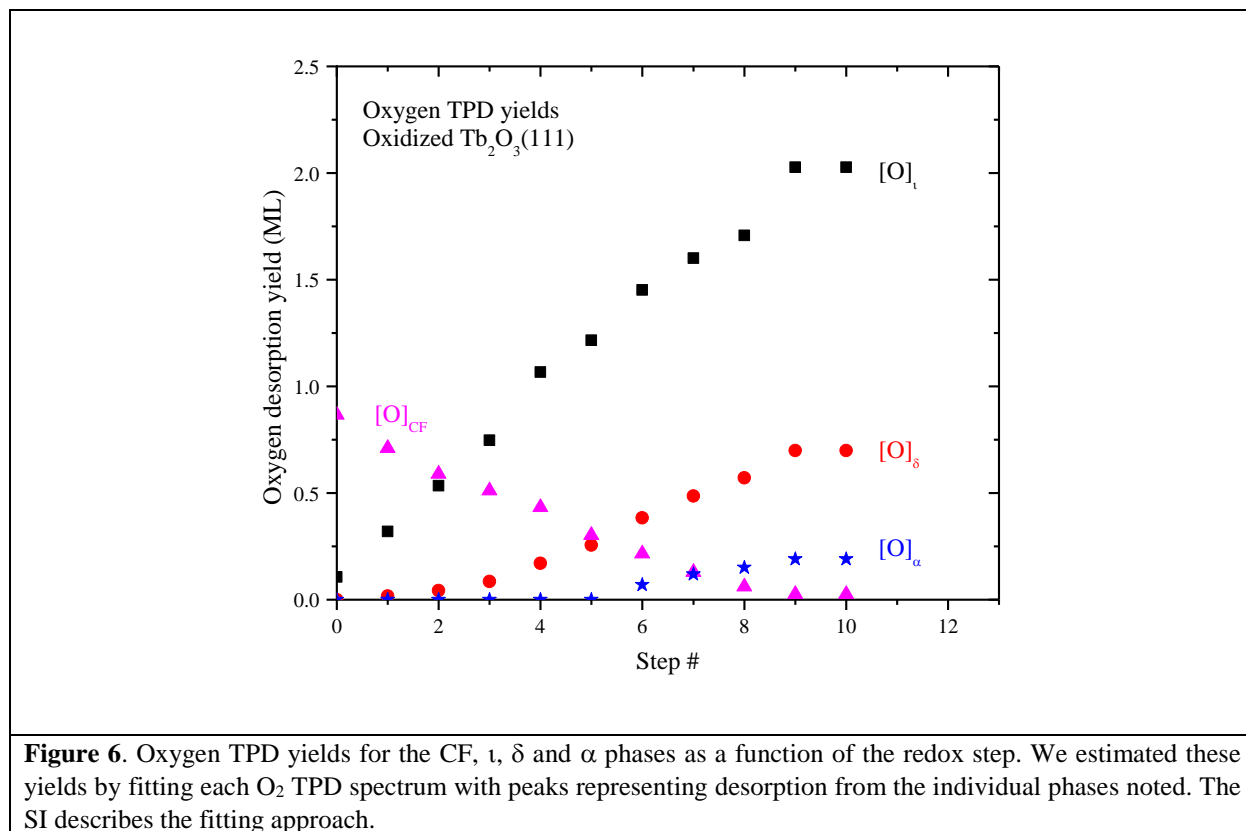
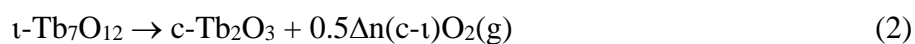


Figure 6 shows the oxygen TPD yield for each oxidized phase as a function of the redox step as computed from the analysis. We find that the desorption yield from oxidized CF- TbO_x decreases steadily with successive redox steps from ~ 0.9 to 0.03 ML, while yields from the ι , δ and α phases concurrently increase and plateau at the tenth step. The results also show that formation of the ι -phase initiates at the outset whereas formation of the more oxidized δ and α phases is delayed, with δ -phase formation initiating before α -phase formation (Figure 6). This behavior demonstrates that a higher oxide begins to form only after a sufficient amount of the next lower oxide is present. For example, the ι -phase develops before the δ -phase forms, and the δ -phase develops before we observe oxygen desorption from the α -phase. A viable explanation is that formation of a higher oxide begins to occur only after domains of the lower oxide become sufficiently large.

We further analyzed the data to estimate the quantities of the ι and δ phases that form during each oxidation step of the c-Tb₂O₃ phase. The analysis is guided by the TbO_x-O₂ phase diagram which shows that the ι and δ phases are stoichiometric compounds at moderate temperature and that a variable-density α -TbO_x phase forms at higher oxygen concentrations, i.e., $x > 1.818$.^{18,55,56} The ι -phase is more stable than the δ -phase and transforms directly to the α -phase at temperatures above the stability limit of the δ -phase. The sharpness of the δ and ι TPD peaks supports the idea that decomposition of the δ and ι phases during TPD generates lower oxides of well-defined stoichiometry, while the broader α TPD feature is consistent with a continuous decrease in the oxygen concentration of an α -TbO_x phase. The successive development of the ι , δ and α TPD features further suggests that these phases form sequentially in order of increasing oxidation state as $c \rightarrow \iota$, $\iota \rightarrow \delta$ and $\delta \rightarrow \alpha$, consistent with the bulk phase diagram. Direct oxidation of the ι -phase to α -TbO_x may also contribute, if, for example, kinetics begins to hinder the vacancy-ordering processes associated with the $\iota \rightarrow \delta$ transformation.

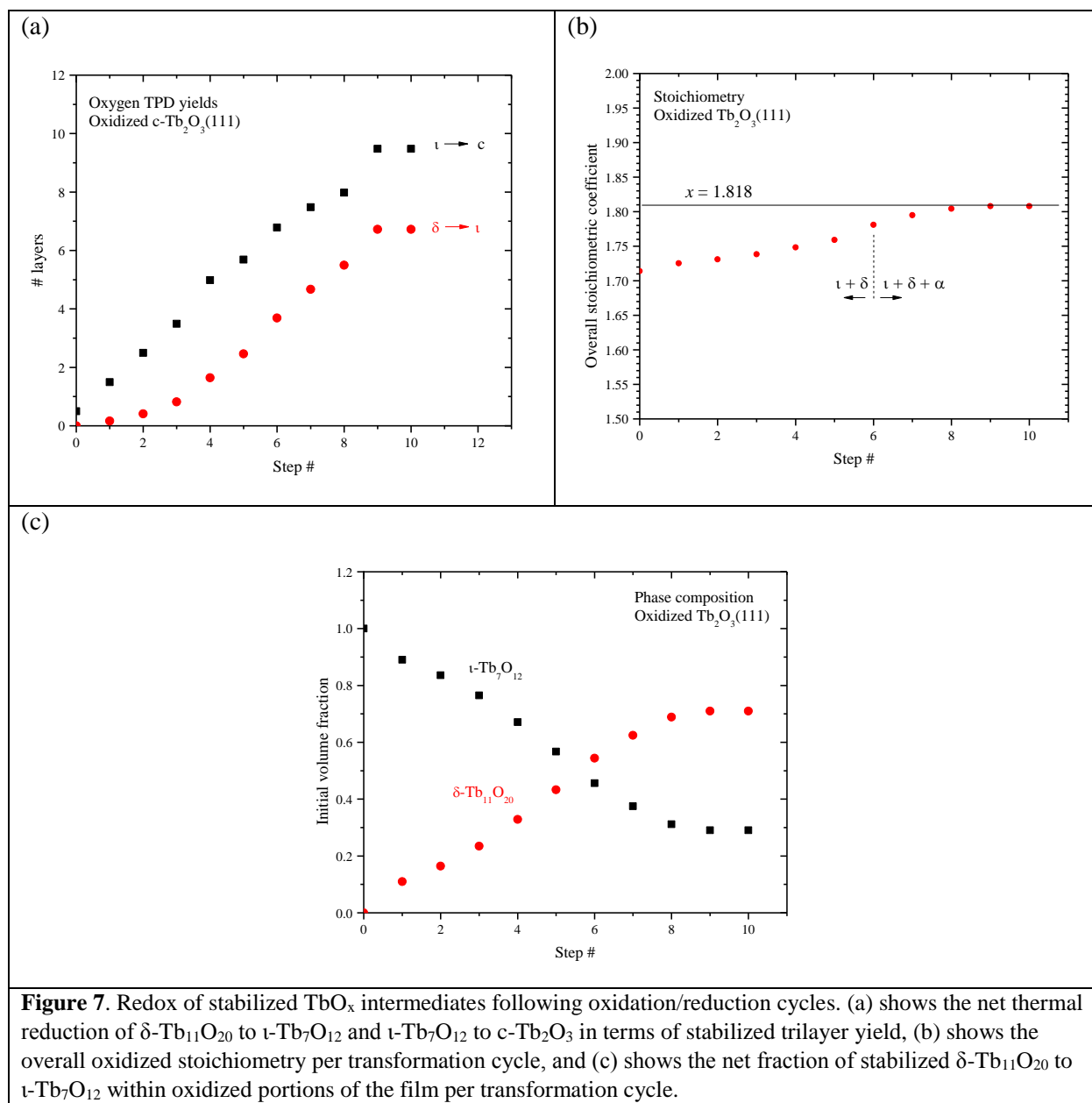
Our analysis focuses on estimating the quantities of the ι and δ phases that decompose during TPD as well as the initial volume fractions of these phases prior to decomposition. We assume that decomposition of the ι and δ phases occurs by the following reactions,



where $\Delta n(\iota\text{-}\delta)$ and $\Delta n(\text{c-}\iota)$ represent the number of moles of oxygen released during the $\delta \rightarrow \iota$ and $\iota \rightarrow \text{c}$ decomposition reactions, and are equal to 0.104 and 0.214 moles, respectively. Given the reaction stoichiometries, we can estimate the quantities of the ι and δ phases that decompose during

TPD which we write in terms of an equivalent number of terbium layers. For example, decomposition of a “layer” of ι -Tb₇O₁₂ to δ -Tb₂O₃ involves a decrease of $\Delta n(c-\iota) = 0.214$ ML of O-atoms. Thus, the total number of ι -phase and δ -phase layers that decompose are given by $L_\iota = [O]_\iota/\Delta n(c-\iota)$ and $L_\delta = [O]_\delta/\Delta n(\iota-\delta)$, respectively, where $[O]_\iota$ and $[O]_\delta$ are the oxygen desorption yields in the ι and δ TPD peaks.

Figure 7a shows the number of layers of the ι and δ -phases that decompose as a function of the redox step according to our analysis. These results show that the ι -phase quantity increases approximately linearly by $\sim 1 \pm 0.3$ layers per redox step. The results further reveal that the amount of ι -phase that decomposes remains greater than the amount of δ -phase that decomposes at each redox step, including the final step when the CF to bixbyite transformation appears to stabilize. We estimate that 9.5 layers of ι -phase decompose after the tenth redox step whereas only 6.7 layers of δ -phase decompose. Our finding that $L_\delta < L_\iota$ indicates that only a fraction of the ι -Tb₇O₁₂ region oxidizes to δ -Tb₁₁O₂₀. Furthermore, the appearance of the α TPD feature suggests that a disordered, oxygen-rich α -TbO_x phase begins to form before the entire region occupied by the ι -phase oxidizes to the δ -phase.



We thus conclude that oxidation and subsequent heating during TPD generates an oxidized region of the film that initially contains L_1 layers of pure $\epsilon\text{-Tb}_7\text{O}_{12}$. Continued oxidation begins to transform $\epsilon\text{-Tb}_7\text{O}_{12}$ to $\delta\text{-Tb}_{11}\text{O}_{20}$, but an oxygen-rich $\alpha\text{-TbO}_x$ phase starts to form before the $\epsilon \rightarrow \delta$ reaction reaches completion. Formation of the $\alpha\text{-TbO}_x$ phase may involve oxidation of the ϵ or δ -phase or both. Incomplete transformation of the ϵ to δ -phase at the onset of α -phase formation

suggests that kinetic factors begin to hinder vacancy-ordering during δ -phase formation once the oxygen content of the film becomes sufficiently high. We illustrate the proposed oxide phase development in a schematic shown in Figure 8.

We also estimated the average oxygen content as well as the initial volume fractions of the ι and δ phases in the oxidized c-Tb₂O₃ region. Our analysis assumes that the total number of layers of c-Tb₂O₃ that oxidizes (L) is equal to the number of layers of ι -phase that decomposes during TPD, i.e., $L = L_{\iota}$. Under this assumption, the initial volume fractions occupied by the ι and δ -phases are given by $f_{\iota} = (L_{\iota} - L_{\delta})/L_{\iota}$ and $f_{\delta} = L_{\delta}/L_{\iota}$ where we define these “initial” fractions as representing the phase composition immediately before α -phase formation. We further define an average oxygen concentration per layer of the entire oxidized c-Tb₂O₃ region as $[O]_{\text{avg}} = ([O]_{\iota} + [O]_{\delta} + [O]_{\alpha})/L$, and express this quantity in terms of an average stoichiometric coefficient for TbO _{x} as $x = 1.5 + [O]_{\text{avg}}$. This definition assumes that the δ and α phases form only within the region of the film that initially oxidizes to the ι -phase, which is reasonable.

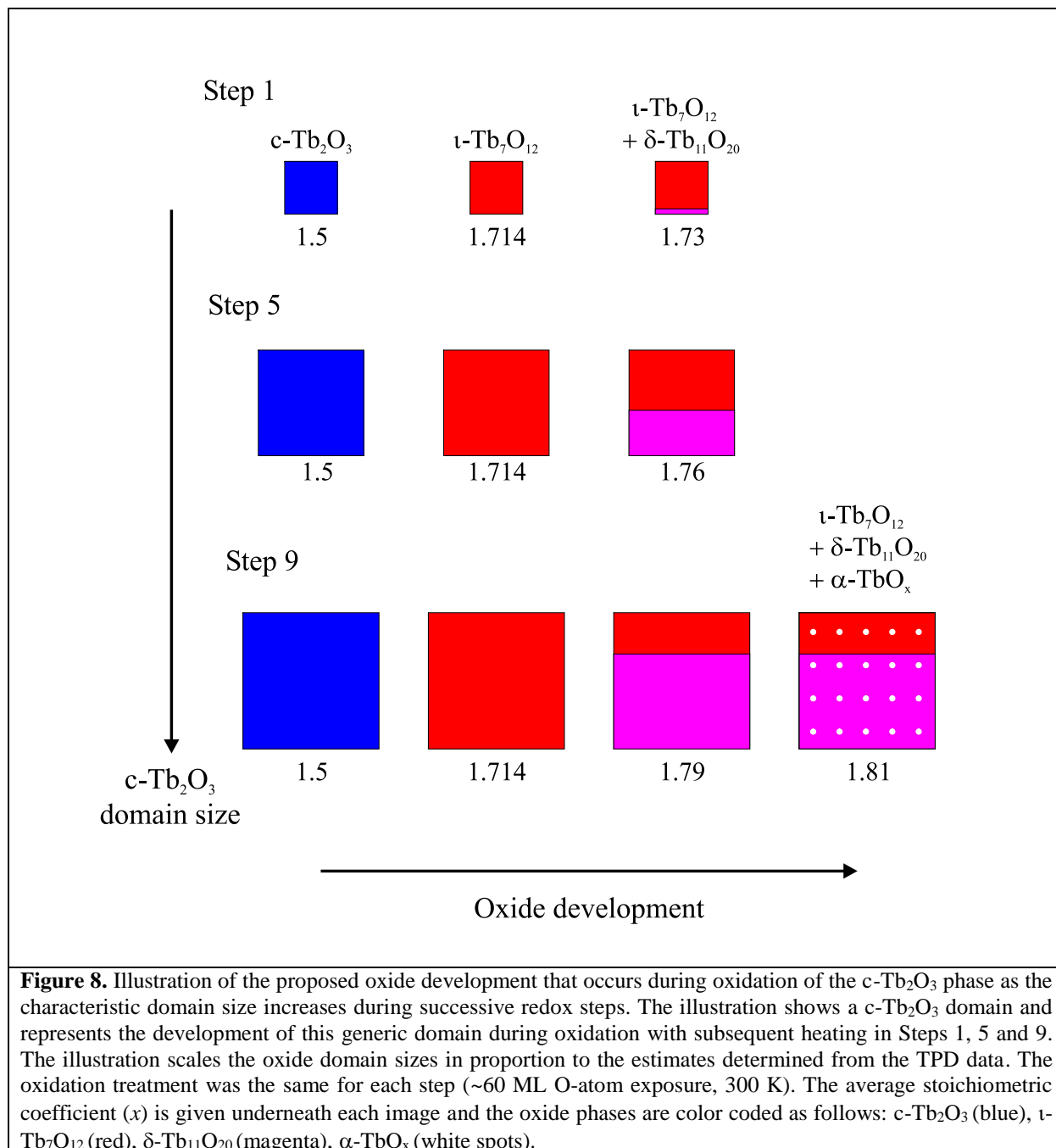
Figure 7b shows that the average stoichiometric coefficient of the oxidized c-Tb₂O₃ region increases from $x = 1.714$ to 1.808 with repeated oxidation/reduction steps. This result indicates that the rate of c-Tb₂O₃ oxidation increases as the total quantity of c-Tb₂O₃ in the film increases, with the initial and final oxygen uptake equal to 0.214 and 0.308 ML of oxygen per layer, respectively. This is an intriguing result as it suggests that c-Tb₂O₃ oxidation becomes increasingly facile as the average c-Tb₂O₃ domain size increases. We marked the sixth step in Figure 7b to illustrate that the α -phase begins to form at an average stoichiometric coefficient of $x = 1.78$, i.e., below that for complete conversion of the ι to δ -phase. We estimate that 6.8 layers of the ι -phase are present at the sixth step, and find that 0.38 ML of oxygen desorbs in the δ TPD feature. This

TPD yield is 0.32 ML less than the amount of oxygen that would desorb in the δ TPD feature if the $\iota \rightarrow \delta$ conversion reached completion, and well below the uncertainty in the O_2 TPD yields, thus supporting the conclusion that the α -state begins to populate before the $\iota \rightarrow \delta$ reaction reaches completion. Our finding that the rate of oxidation increases as the quantity of c-Tb₂O₃ increases suggests that the relation between the total oxygen uptake and the redox step should exhibit an increasing slope (i.e., concave upward), provided that the amount of c-Tb₂O₃ in the film increases by a constant amount during each reduction step. However, a change in the slope is too gradual to resolve in our data, and lies within the variation in the total amount by which the c-Tb₂O₃ increases in each step (1 ± 0.3 layers/step).

Figure 7c shows that the initial volume fraction of the ι -phase decreases steadily from 100% to 30% with successive redox steps, while the initial volume fraction of the δ -phase concurrently increases, reaching 70% at the ninth step. This result shows that an increasing quantity of the ι -phase oxidizes to the δ -phase as the quantity of c-Tb₂O₃ in the film increases and the CF to bixbyite transformation approaches completion. We speculate that vacancy-ordering associated with the $\iota \rightarrow \delta$ conversion is more facile for larger domains of the crystalline ι -phase. As a result, the extent of oxidation and the δ -phase volume fraction increase as the c-Tb₂O₃ domains grow in size during the repeated oxidation/reduction treatment.

Figure 8 provides a representative schematic illustrating how the oxide phases develop during oxidation and subsequent heating of the c-Tb₂O₃ phase, according to our analysis, as the amount of c-Tb₂O₃ in the film increases in successive redox steps. Figure 8 represents these changes for Steps 1, 5 and 9, and scales the sizes of the oxide domains in proportion to the amounts determined from our analysis of TPD data. The different oxide phases are color coded and the average

stoichiometric coefficient is given underneath each image in Figure 8. Our results provide evidence that the characteristic c-Tb₂O₃ domain size increases after each redox step, and that the extent to which the c-Tb₂O₃ phase oxidizes during a fixed O-atom exposure increases with increasing domain size. Further, as mentioned above, we contend that the c-Tb₂O₃ phase completely transforms to the ι -Tb₇O₁₂ phase for each oxidation and heating step, whereas oxidation beyond the ι -phase stoichiometry ($x = 1.714$) depends on the average domain size. Our illustration depicts the δ -phase as forming at the buried interface of the ι -Tb₇O₁₂ domain. This representation of the spatial profile of the oxide phases is speculative, yet also inconsequential to the main conclusions of the present study.



Following our TPD analysis, Figure 8 shows that complete transformation of $c\text{-Tb}_2\text{O}_3$ to $\iota\text{-Tb}_7\text{O}_{12}$ is followed by oxidation of a small portion of the ι -phase to $\delta\text{-Tb}_{11}\text{O}_{20}$ during Step 1, resulting in final volume fractions of $f_{\iota} = 0.90$ and $f_{\delta} = 0.10$ and an average stoichiometric coefficient of $x = 1.73$. We estimate that the amount of the $c\text{-Tb}_2\text{O}_3$ phase in the film increased

from 1.5 to 5.7 layers between Steps 1 and 5, and represent this change as a proportional increase in the $c\text{-Tb}_2\text{O}_3$ domain size. Figure 8 also shows that the δ -phase occupies a larger fraction of the domain after oxidation at Step 5 compared with Step 1. Specifically, we estimate that oxidation at Step 5 produces an oxidized region with 57% $\iota\text{-Tb}_7\text{O}_{12}$ and 43% $\delta\text{-Tb}_{11}\text{O}_{20}$ (i.e., $f_\iota = 0.57$, $f_\delta = 0.43$), and an average stoichiometric coefficient of $x = 1.76$. Finally, we show that the ι phase oxidizes to the δ -phase during Step 9, but that the $\iota \rightarrow \delta$ reaction ceases and the α -phase develops instead once $f_\delta \sim 0.70$. We illustrate the α -phase in Figure 8 as distributed between both the ι and δ phases but note that such a distribution is speculative. It is possible that the α -phase develops preferentially within either the ι or δ -phase, but we are unable to make such a distinction from the current data.

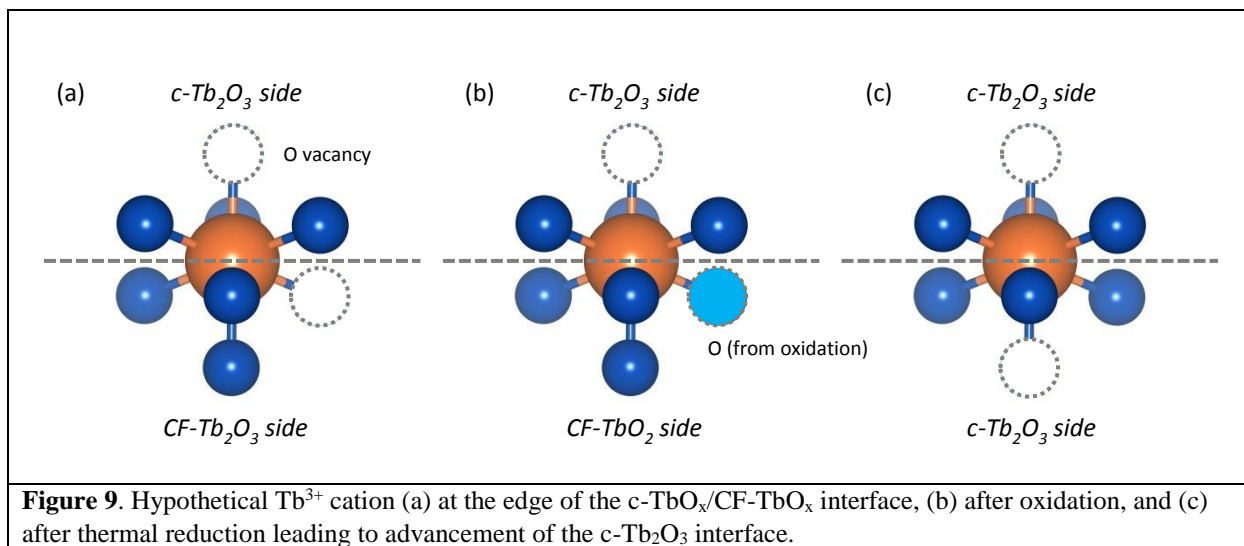
Discussion

Redox-induced structural transformation

Our results show that repeated oxidation and thermal reduction to 1000 K causes an oxygen-deficient $\text{CF-Tb}_2\text{O}_3$ film to transform to the well-ordered $c\text{-Tb}_2\text{O}_3$ structure. The addition and removal of lattice oxygen plays a decisive role in facilitating this transformation given that annealing the $\text{CF-Tb}_2\text{O}_3$ film to 1000 K is insufficient to reorder the existing Tb-O bonds and achieve the long-range vacancy ordering that characterizes the bixbyite structure.¹⁶ The continual increase in lattice oxygen accommodated by the film over the course of the transformation is consistent with an increasing quantity of $c\text{-Tb}_2\text{O}_3$ domains within the film as well as more facile oxidation of $c\text{-Tb}_2\text{O}_3$ to $\iota\text{-Tb}_7\text{O}_{12}$ and $\delta\text{-Tb}_{11}\text{O}_{20}$. This observation suggests a mechanism in which $c\text{-Tb}_2\text{O}_3$ seeds form within the near surface region of the CF-TbO_x film and continue to propagate

across the buried c-Tb₂O₃/CF-Tb₂O₃ interface, particularly during thermal reduction between 900-1000 K. The similarity in the amount of oxygen desorbed and the amount of CF-Tb₂O₃ converted to c-Tb₂O₃ between ~900-1000 K suggests that oxygen removal in this temperature regime is particularly effective in promoting the CF-Tb₂O₃ to c-Tb₂O₃ transformation.

While determining the exact mechanism for the redox-induced conversion of CF to bixbyite Tb₂O₃ is challenging, we speculate that the avoidance of low Tb oxidation states (< +3) is important in facilitating the CF-to-bixbyite transformation via the redox mechanism compared with vacancy reordering in CF-Tb₂O₃. We illustrate this general idea using a hypothetical structure of a TbO₆ moiety located at the CF-Tb₂O₃/c-Tb₂O₃ interface (Figure 9a), and represent the CF-Tb₂O₃ to c-Tb₂O₃ transformation as a change in the O-vacancy site located in the initial CF-Tb₂O₃ side of the interface. In this model, a direct structural rearrangement involves the hopping of an O-vacancy between sites on the CF-Tb₂O₃ side of the interface, transforming the moiety to bixbyite. This process causes neighboring Tb cations to become reduced to the nominal +2.5 oxidation state and should thus be energetically demanding given the high stability of Tb⁺³ vs. Tb⁺².^{18,57} In the redox-induced mechanism, an O-atom enters the vacancy on the CF-side of the interface, and an O-atom subsequently vacates a different, nearby site to transform the entire moiety to c-Tb₂O₃ (Figure 9b,c). The Tb oxidation state nominally changes from +3.5 to +3 during the reduction step depicted in Figure 9, and thereby avoids reduction below the +3 state. An analogous mechanism is that O-atoms sequentially fill a vacancy on the c-Tb₂O₃ side and then the CF-Tb₂O₃ side to generate a TbO₂ moiety, and that O-atoms vacate the apical sites shown in Figure 9 during reduction and convert the entire moiety to c-Tb₂O₃. We assert that preservation of the Tb⁺³/Tb⁺⁴ oxidation states during the redox-mechanism is significant in lowering the energetic requirements for vacancy reordering and formation of c-Tb₂O₃.



The high temperatures ($>\sim 900$ K) needed to promote the redox-mechanism for $c\text{-Tb}_2\text{O}_3$ formation are likely associated with accommodation of O-atoms into the terbia lattice after the oxidation step. The O-atoms added to the lattice are unlikely to fully relax into optimal bonding configurations at the low oxidation temperature employed (300 K). As a result, the added O-atoms are less stable than the original lattice O-atoms and preferentially vacate their binding sites during thermal reduction, restoring the oxide to the $\text{CF-Tb}_2\text{O}_3$ structure. At higher temperatures, the lattice can more fully relax and enable the added O-atoms to achieve similar stability as the original lattice oxygen. Once the added O-atoms are stabilized, it should be favorable to remove one of the original lattice O-atoms to generate the more stable bixbyite structure. A similar transition is observed during the slow reduction of $\text{CeO}_2(111)$ with H_2 at 700 K where the surface retains a high degree of homogeneity and crystallinity during the progression through the (1×1) fluorite CeO_2 , (3×3) partially reduced CeO_x , and fully reduced (4×4) bixbyite Ce_2O_3 structures.³⁸ We emphasize that our arguments are speculative and that future computational modeling could aid in clarifying the elementary steps and energetics associated with the redox mechanism for $c\text{-Tb}_2\text{O}_3$ formation.

Thickness of the c-Tb₂O₃ region

Our results provide evidence that only the top layers of the film become oxidized and transform from the CF to bixbyite structure during reduction. We specifically estimate a Tb₂O₃ film thickness of ~18 layers from measurements of the Pt 4f peak attenuation, whereas our O₂ TPD results indicate that about 10 layers near the vacuum-solid interface transformed to c-Tb₂O₃. These estimates suggest that the final reduced film consists of ~10 layers of c-Tb₂O₃(111) on top of 8 layers of oxygen-deficient CF-Tb₂O₃(111). Experimental uncertainty in our estimates is unlikely to account for such a large difference between the thickness of the entire film and the region that oxidizes and transforms to bixbyite. For example, the IMFP of Pt 4f photoelectrons needs to be lowered to ~55% of the estimated value (15 vs. 27 Å) to predict a film thickness that equals the thickness of the oxidized region that we determine from the oxygen uptake. An error of this magnitude is physically unreasonable. Further, we estimate an uncertainty of less than 10% in the oxygen coverages determined from the O₂ TPD yields. We thus conclude that the final film does in fact include a buffer region of CF-Tb₂O₃ separating the c-Tb₂O₃(111) phase from the Pt(111) substrate.

We have previously reported that CF-Tb₂O₃(111) grows epitaxially on Pt(111) and adopts an (3 × 3)/(4 × 4) coincident structure with minimal strain due to good lattice matching between the oxide and Pt(111). In contrast, c-Tb₂O₃(111) has a lattice constant that is about 5.5 times larger than that of Pt(111) and would thus experience significant strain as a commensurate layer. The c-Tb₂O₃(111) structure can adopt a (4 × 4) structure on CF-TbO_x(111). The favorable epitaxial relationship between CF-Tb₂O₃(111) and Pt(111) may play a key role in limiting the thickness of the c-Tb₂O₃(111) region that forms by repeated oxidation and reduction of the Tb₂O₃ film. Specifically, we assert that only the top layers of the CF-Tb₂O₃ film transform to c-Tb₂O₃ in order

to maintain a region of CF-Tb₂O₃ between the c-Tb₂O₃ phase and the Pt(111) substrate that acts to mitigate strain in the oxide film.

Summary

We used O₂ TPD and LEED to investigate the transformation of a Tb₂O₃(111) thin film from the cubic fluorite to bixbyite structure, as induced by repeated oxidation at 300 K and thermal reduction by heating to 1000 K. The CF to c-Tb₂O₃ conversion occurs in a stepwise fashion and discontinues after the formation of ~10 layers of c-Tb₂O₃(111) at the surface for the conditions studied. Our results suggest that the final reduced film consists of a region of c-Tb₂O₃(111) that is separated from the Pt(111) substrate by about eight layers of CF-Tb₂O₃(111). We show that oxidation of the c-Tb₂O₃(111) phase occurs through successive formation of the ι -Tb₇O₁₂ and δ -Tb₁₁O₂₀ phases, and a variable-density α -TbO_x phase with high oxygen content ($x > \sim 1.8$). The total oxygen uptake increases as the quantity of c-Tb₂O₃ increases, demonstrating that the c-Tb₂O₃ phase oxidizes more efficiently than the oxygen-deficient CF-Tb₂O₃ phase. Our results provide evidence that the CF to bixbyite transformation occurs mainly above ~900 K as the oxidized TbO_x film undergoes thermal reduction. We suggest that c-Tb₂O₃ regions form at phase interfaces during TbO_x reduction, with this process enabling newly formed c-Tb₂O₃ to advance deeper into the film.

Supporting Information

O₂ TPD data obtained after the CF to bixbyite transformation; Estimates of oxide-phase quantities from O₂ TPD fits.

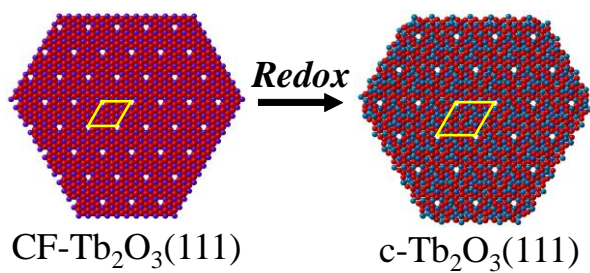
Acknowledgements

We thank Sangmyeon Lee, Ankit Gokhale, and Mohammed Shariff for assistance with experiments. We gratefully acknowledge financial support for this work provided by the National Science Foundation, Division of Chemistry through grant number 1464765.

References

1. S. Colussi, C. de Leitenburg, G. Dolcetti and A. Trovarelli, *J. Alloys Compd.*, 2004, **374**, 387-392.
2. A. Schaefer, W. Cartas, R. Rai, M. Shipilin, L. R. Merte, E. Lundgren and J. F. Weaver, *J. Phys. Chem. C*, 2016, **120**, 28617-28629.
3. J. Graciani, K. Mudiyansele, F. Xu, A. E. Baber, J. Evans, S. D. Senanayake, D. J. Stacchiola, P. Liu, J. Hrbek, J. F. Sanz and J. A. Rodriguez, *Science*, 2014, **345**, 546-550.
4. G. Vile, B. Bridier, J. Wichert and J. Perez-Ramirez, *Angew. Chem. Int. Ed. Engl.*, 2012, **51**, 8620-8623.
5. J.-H. Jhang, A. Schaefer, V. Zielasek, J. Weaver and M. Bäumer, *Materials*, 2015, **8**, 6228-6256.
6. A. G. Dedov, A. S. Loktev, I. I. Moiseev, A. Aboukais, J. F. Lamonier and I. N. Filimonov, *Appl. Catal., A*, 2003, **245**, 209-220.
7. O. Forlani and S. Rossini, *Mater. Chem. Phys.*, 1992, **31**, 155-158.
8. T. W. Elkins and H. E. Hagelin-Weaver, *Appl. Catal., A*, 2013, **454**, 100-114.
9. T. W. Elkins, B. Neumann, M. Bäumer and H. E. Hagelin-Weaver, *ACS Catal.*, 2014, **4**, 1972-1990.
10. T. W. Elkins, S. J. Roberts and H. E. Hagelin-Weaver, *Appl. Catal., A*, 2016, **528**, 175-190.
11. S. H. Overbury, D. R. Mullins, D. R. Huntley and L. Kundakovic, *J. Catal.*, 1999, **186**, 296-309.
12. R. M. Ferrizz, T. Egami, G. S. Wong and J. M. Vohs, *Surf Sci.*, 2001, **476**, 9-21.
13. Z. Yang, T. K. Woo and K. Hermansson, *Surf Sci.*, 2006, **600**, 4953-4960.
14. J.-H. Jhang, A. Schaefer, W. Cartas, S. Epuri, M. Bäumer and J. F. Weaver, *J. Phys. Chem. C*, 2013, **117**, 21396-21406.
15. W. Cartas, R. Rai, A. Sathe, A. Schaefer and J. F. Weaver, *J. Phys. Chem. C*, 2014, **118**, 20916-20926.
16. C. Lee, V. Mehar and J. F. Weaver, *J. Phys. Chem. C*, 2018, **122**, 9997-10005.
17. A. Schaefer, B. Hagman, J. Höcker, U. Hejral, J. I. Flege and J. Gustafson, *Phys. Chem. Chem. Phys.*, 2018, **20**, 19447-19457.
18. G.-y. Adachi and N. Imanaka, *Chem. Rev.*, 1998, **98**, 1479-1514.
19. J. Höcker, T. Duchoň, K. Veltruská, V. Matolín, J. Falta, S. D. Senanayake and J. I. Flege, *J. Phys. Chem. C*, 2016, **120**, 4895-4901.
20. T. Duchoň, J. Hackl, J. Höcker, K. Veltruská, V. Matolín, J. Falta, S. Cramm, S. Nemšák, C. Schneider, J. Flege and S. Senanayake, *Ultramicroscopy*, 2017, **183**, 84-88.
21. Y. Takasu, T. Yoko-o, M. Matsui, Y. Matsuda and I. Toyoshima, *J. Catal.*, 1982, **77**, 485-490.
22. A. Trovarelli, *Catalysis Reviews*, 1996, **38**, 439-520.
23. D. R. Mullins, *Surf. Sci. Rep.*, 2015, **70**, 42-85.
24. G. V. Antoshin, K. M. Minachev and R. V. Dmitriev, *Bulletin of the Academy of Sciences of the USSR, Division of Chemical Science*, 1967, **16**, 1793-1795.
25. P. Kunzmann and L. Eyring, *J. Solid State Chem.*, 1975, **14**, 229-237.

26. V. Matolín, J. Libra, I. Matolínová, V. Nehasil, L. Sedláček and F. Šutara, *Appl. Surf. Sci.*, 2007, **254**, 153-155.
27. P. Luches, F. Pagliuca and S. Valeri, *J. Phys. Chem. C*, 2011, **115**, 10718-10726.
28. S. Eck, C. Castellarin-Cudia, S. Surnev, M. G. Ramsey and F. P. Netzer, *Surf Sci.*, 2002, **520**, 173-185.
29. D. C. Grinter, R. Ithnin, C. L. Pang and G. Thornton, *J. Phys. Chem. C*, 2010, **114**, 17036-17041.
30. L. H. Chan and J. Yuhara, *J. Chem. Phys.*, 2015, **143**, 074708.
31. M. Alexandrou and R. M. Nix, *Surf Sci.*, 1994, **321**, 47-57.
32. F. Faisal, A. Toghan, I. Khalakhan, M. Vorokhta, V. Matolin and J. Libuda, *Appl. Surf. Sci.*, 2015, **350**, 142-148.
33. D. R. Mullins, S. D. Senanayake and T. L. Chen, *J. Phys. Chem. C*, 2010, **114**, 17112-17119.
34. J. Höcker, J.-O. Krisponeit, T. Schmidt, J. Falta and J. I. Flege, *Nanoscale*, 2017, **9**, 9352-9358.
35. V. Stetsovych, F. Pagliuca, F. Dvorak, T. Duchon, M. Vorokhta, M. Aulicka, J. Lachnitt, S. Schernich, I. Matolinova, K. Veltruska, T. Skala, D. Mazur, J. Myslivecek, J. Libuda and V. Matolin, *J Phys Chem Lett*, 2013, **4**, 866-871.
36. T. Duchoň, F. Dvořák, M. Aulická, V. Stetsovych, M. Vorokhta, D. Mazur, K. Veltruská, T. Skála, J. Mysliveček, I. Matolínová and V. Matolín, *J. Phys. Chem. C*, 2014, **118**, 357-365.
37. P. Luches, G. Gasperi, M. Sauerbrey, S. Valeri, J. Falta and J. I. Flege, *Frontiers in Chemistry*, 2019, **7**.
38. J. Höcker, T. O. Menteş, A. Sala, A. Locatelli, T. Schmidt, J. Falta, S. D. Senanayake and J. I. Flege, *Adv. Mater. Interf.*, 2015, **2**, 1500314.
39. T. Weisemoeller, F. Bertram, S. Gevers, A. Greuling, C. Deiter, H. Tobergte, M. Neumann, J. Wollschläger, A. Giussani and T. Schroeder, *J. Appl. Phys.*, 2009, **105**, 124108.
40. H. Wilkens, S. Gevers, S. Röhe, A. Schaefer, M. Bäumer, M. H. Zoellner, T. Schroeder and J. Wollschläger, *J. Phys. Chem. C*, 2014, **118**, 3056-3061.
41. T. Schroeder, P. Zaumseil, G. Weidner, C. Wenger, J. Dabrowski, H.-J. Müssig and P. Storck, *J. Appl. Phys.*, 2006, **99**, 014101.
42. T. Weisemoeller, C. Deiter, F. Bertram, S. Gevers, A. Giussani, P. Zaumseil, T. Schroeder and J. Wollschläger, *Appl. Phys. Lett.*, 2008, **93**, 032905.
43. A. Schaefer, S. Gevers, V. Zielasek, T. Schroeder, J. Falta, J. Wollschlager and M. Baumer, *J. Chem. Phys.*, 2011, **134**, 054701.
44. H. H. Kan, R. B. Shumbera and J. F. Weaver, *J. Chem. Phys.*, 2007, **126**, 134704.
45. R. Bradley Shumbera, H. H. Kan and J. F. Weaver, *Surf Sci.*, 2007, **601**, 4809-4816.
46. A. L. Gerrard, J.-J. Chen and J. F. Weaver, *J. Phys. Chem. B*, 2005, **109**, 8017-8028.
47. J. Höcker, W. Cartas, A. Schaefer, M. Bäumer, J. F. Weaver, J. Falta and J. I. Flege, *J. Phys. Chem. C*, 2015, **119**, 14175-14184.
48. W. Xiao, Q. Guo and E. G. Wang, *Chem. Phys. Lett.*, 2003, **368**, 527-531.
49. C. J. Powell and A. Jablonski, *Journal*, 2010, **Version 1.2**.
50. K. Otsuka and T. Nakajima, *J. Catal.*, 1987, **103**, 216-219.
51. S. Bernal, J. J. Calvino, G. Cifredo, J. Gatica, C. Larese and J. M. Pintado, *J. Alloys Compd.*, 1995, **225**, 633-637.
52. H. Wilkens, O. Schuckmann, R. Oelke, S. Gevers, A. Schaefer, M. Bäumer, M. H. Zoellner, T. Schroeder and J. Wollschläger, *Appl. Phys. Lett.*, 2013, **102**, 111602.
53. R. Olbrich, G. E. Murgida, V. Ferrari, C. Barth, A. M. Llois, M. Reichling and M. V. Ganduglia-Pirovano, *J. Phys. Chem. C*, 2017, **121**, 6844-6851.
54. G. Gasperi, L. Amidani, F. Benedetti, F. Boscherini, P. Glatzel, S. Valeri and P. Luches, *Phys. Chem. Chem. Phys.*, 2016, **18**, 20511-20517.
55. H. Inaba, A. Navrotsky and L. Eyring, *J. Solid State Chem.*, 1981, **37**, 77-84.
56. L. Eyring, in *Synthesis of Lanthanide and Actinide Compounds*, eds. G. Meyer and L. R. Morss, Springer Netherlands, Dordrecht, 1991, pp. 187-224.
57. J. M. Leger, N. Yacoubi and J. Loriers, *J. Solid State Chem.*, 1981, **36**, 261-270.



Repeated oxidation and reduction transforms a cubic fluorite Tb₂O₃(111) film to the bixbyite structure.